Actuators **2015**, *4*, 217-236; doi:10.3390/act4040217

OPEN ACCESS

actuators

ISSN 2076-0825

www.mdpi.com/journal/actuators

Article

Design and Characterization of a High-Precision Digital Electromagnetic Actuator with Four Discrete Positions

Laurent Petit *, Erwan Dupont, Emmanuel Doré, Frédéric Lamarque and Christine Prelle

Sorbonne Universités, Université de Technologie de Compiègne, CNRS, UMR 7337 Roberval, Centre de recherche Royallieu, CS 60319, 60203, Compiègne cedex, France;
E-Mails: erwan.dupont@utc.fr (E.D.); emmanuel.dore@utc.fr (E.D.); frederic.lamarque@utc.fr (F.L.); christine.prelle@utc.fr (C.P.)

***** Author to whom correspondence should be addressed; E-Mail: laurent.petit@utc.fr; Tel.: +33-344-234-587.

Academic Editors: Micky Rakotondrabe and Mathieu Grossard

Received: 26 August 2015 / Accepted: 16 October 2015 / Published: 21 October 2015

Abstract: A high-precision planar digital electromagnetic actuator with two displacement directions and four discrete positions is presented in this paper. The four discrete positions are located at each corner of a square cavity where a mobile permanent magnet moves thanks to Lorentz forces generated when a driving current passes through two orthogonal wires placed below the cavity. Four fixed permanent magnets are placed around the cavity in order to ensure high-precision magnetic holding of the mobile magnet at each discrete position. An analytical model of the actuator is presented and used to characterize its properties (switching time, energy consumption, and displaceable mass). Based on this model, an experimental prototype has been developed and then characterized. Comparisons between experimental and simulated results are carried out and show good agreement. The positioning repeatability errors have also been characterized according to the input signal in order to qualify the digital behavior of this high-precision actuator. Finally, an application of this digital actuator as a linear conveyor is presented and experimentally tested.

Keywords: electromagnetic actuator; digital mechanism; two-dimensional displacements; conveyance device

---

1. Introduction

To realize high-resolution tasks, analog actuators are generally employed [1,2]. These actuators are able to realize continuous motions within their working stroke limits. In literature, many analog actuators have been developed to realize, as well as planar [1,3], rotary [4–6] or combined motions [7]. Sensory components need to be integrated for the control of these actuators in order to ensure high resolution positioning or precise trajectories [7,8]. The control laws are generally complex, according to the high-performance levels needed. Moreover in highly integrated or compact mechatronic systems, the integration of sensory components is sometimes difficult or even impossible. For these reasons, actuators based on a digital principle are one of the interesting alternatives.

Digital (or binary) actuators consist of a mobile part able to switch between repeatable and well known discrete positions. The main advantage of digital actuators is that an internal energy holding of the mobile part in discrete position is provided so that external energy supply (pulses) is only needed to switch the mobile part between the discrete positions [9]. It provides several interests. Firstly, this pulse mode control ensures a low energy consumption because there is no need of energy to hold the mobile part in discrete position [10,11]. The control can also lead to a very simple open loop binary control [12,13] because the digital actuation ensures highly repeatable and accurate discrete positions which do not need external measurement systems [14]. The integration of these actuators in mechanical or mechatronic systems is then easy. In addition, digital outputs of a data acquisition board can be used to control digital actuators instead of analog outputs needed for analog actuators, which decreases the total cost of the system. Another advantage of this pulse mode is the reduction of the Joule effect due to the short duration of the control pulse [15].

However due to their digital principle, digital actuators present some limitations and requirements. The main limitation is relative to their discrete stroke fixed at the manufacturing step. In standard functioning, the mobile part of digital actuators can indeed not stop in an intermediate position located between two discrete positions. This limitation can be overcome since variable strokes can been achieved using an assembly of several digital actuators [12]. Otherwise, a crucial requirement to ensure high-precision tasks is the high manufacturing quality required for digital actuators (surface, tolerance, *etc.*) because the influence of manufacturing errors cannot be compensated by a closed loop control.

Two functions are needed to perform digital actuation: the driving function, to switch the mobile part between the discrete positions, and the holding function, to hold the mobile part in discrete position. In literature, the driving function is generally obtained via electrostatic [16], thermal [17,18] electromagnetic [19,20] or piezoelectric [21] physical effects. For the holding function, three commonly used methods are employed, such as magnetic effect [19,20], compliant mechanisms [18,22], and position locking actuators [23].

Due to their simplicity, digital actuators are used in various types of applications which can be classified into two categories. The first one regroups devices composed of a single digital actuator as electrical [11,16], optical [24,25], and fluidic [26,27] switches. The second category includes devices where several actuators are integrated so that complex tasks can be realized by combination of elementary actions. Switches arrays [27], tactile display devices [28], digital-to-analog converters [29], digital robots [12,30], and distributed conveyance devices [31,32] are some examples of these applications.

In this work, a high-precision electromagnetic digital actuator is presented. The electromagnetic principle has been chosen because it is well adapted for digital actuation. As a matter of fact, it can manage both holding and switching functions: a magnetic holding force can be easily obtained using the magnetic property of the mobile permanent magnet while the driving force is obtained electromagnetically (Lorentz force). Compared to the literature, the main originality of the presented digital actuator is that the mobile part can perform displacements along two orthogonal directions without an assembly of two 1D actuators [33]. This configuration reduces the assembly errors, thus enhancing the precision of the actuator and improving its compactness.

A first version of this actuator was previously developed and tested along one axis only [20]. In the presented paper, an optimized and more compact version of the actuator is presented. In a first part, the principle and the architecture of this new version is described. An analytical model of the actuator is used to characterize the energy consumption and the maximal displaceable mass. Then an experimental prototype is presented and tested. Comparisons between experimental and simulated results are carried out. The positioning repeatability errors have been measured to characterize the digital behavior of the actuator and its high-precision property. Finally, an example of application which takes advantage of the two orthogonal displacement directions and the high-precision positioning is described and experimentally tested.

2. Principle

The presented actuator is composed of a mobile part, which is a parallelepiped mobile permanent magnet (MPM), and a fixed part which regroups a square cavity, four fixed permanent magnets (FPMs) and two orthogonal wires (Figure 1). The MPM is placed in a square cavity and can reach its four corners which correspond to the four discrete positions of the actuator. The gap between the MPM and the square cavity characterizes the actuator stroke. Four FPMs, with a magnetization orientated in the opposite direction as compared to the MPM, are placed near each corner so that a magnetic attraction force is exerted on the MPM in discrete position. This magnetic force ensures the holding function which characterizes the positioning repeatability of the MPM in discrete position then the high precision property of the presented actuator. The switching function of the MPM between the discrete positions is obtained using two electrical wires placed below the cavity. When a current passes through a wire, a Lorentz force is generated between the MPM and the wire. Since the wire is fixed, the MPM moves thanks to this force. In order to get an electrical insulation between the two wires, one wire is printed on the top side of a double side printed circuit board (PCB) and second one on the bottom side. The wire placed closed to the MPM (distance d_2 in Figure 1) is called top wire (TW) and is used to switch the MPM along *x*-axis. The second wire placed far away from the MPM (distance d_3 in Figure 1) is called bottom wire (BW) and is used to switch the MPM along *y*-axis. In order to minimize the difference of the Lorentz force generated by the two wires on the MPM, the thickness of the PCB has been chosen as small as possible (200 µm). Moreover, a thin glass layer of 170 µm thickness is placed between MPM and the PCB to avoid electrical contact between the TW and the MPM and provide a flat surface. The geometrical, magnetic, and electromagnetic properties of the actuator are given in Table 1.

In Figure 1, the MPM is located in the discrete position ($-x_{MPM}$; $-y_{MPM}$). If a switch along the $+x$ direction is desired, a driving current should be injected through the "wire for *x*-axis switching" (TW)

in the –*y* direction. This current will generate a Lorentz force on the TW in the –*x* direction due to the orientation of MPM magnetic flux density in the +*z* direction (left hand rule). Since the TW is fixed, an opposite force in the +*x* direction is exerted on the MPM which switches to reach the discrete position ($+x_{MPM}$; $-y_{MPM}$). During this switch, the holding force in the –*y* direction can be increased using a holding current through the "wire for *y*-axis switching" (BW) in the –*x* direction. This increase in the holding force can be interesting to reduce the influence of disruptions during the MPM switch and to increase the positioning precision of the MPM in discrete position.

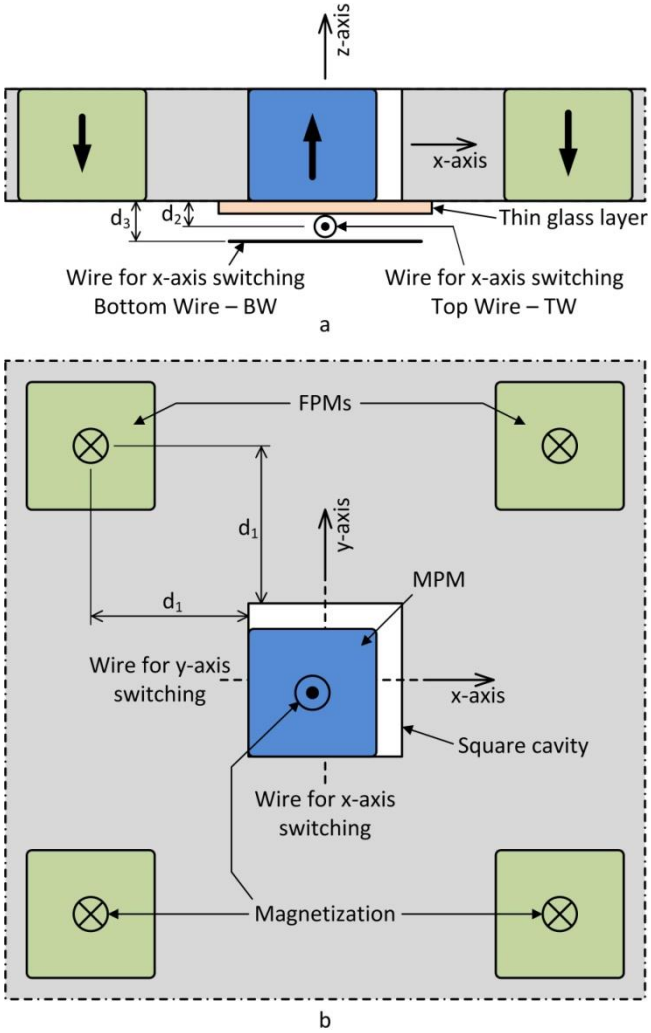

Figure 1. Principle of the four discrete positions actuator: (**a**) side view, and (**b**) top view.

The high-precision property of the actuator is characterized by the magnetic holding force generated by the FPMs on the MPM. An increase of the magnetic holding force ensures a higher positioning precision of the MPM in discrete positions even in the presence of high disturbances; nevertheless, the energy consumption needed to switch from one position to another one will also increase. For the presented actuator, a compromise between the high-precision digital behavior and the minimal driving current value has been accomplished by choosing a holding force of 1 mN. This value is obtained with a distance d_1 of 11 mm (Figure 1). This holding force value has been chosen so that the minimal driving current necessary to switch the MPM is lower than 2 A (without transported mass).

Table 1. Actuator properties.

Distances	
d_1	11 mm
d_2	223 µm
d_3	458 µm
MPM stroke	1 mm
Permanent magnet properties	
Material	Gold-coated NdFeB
Mass	435 ± 1 mg
Dimensions	5 × 5 × 2 mm^3
Magnetization	1.345 T
Magnetic and electromagnetic forces	
Magnetic holding force	1.0 mN
Electromagnetic force	TW: 1.5 mN for 1 A BW: 1.4 mN for 1 A

3. Analytical Model of the Digital Actuator

An analytical model of the actuator implemented with MATLAB software has been developed to compute the forces exerted on the MPM and its displacement along the two displacement axes. With this model, the PMs are considered as parallelepiped blocks (without geometrical and dimensional errors) placed in free space with uniform magnetizations. The calculation of the magnetic and electromagnetic forces is based on the magnetic flux density computed using the charge model [34]. Equation (1) gives the expression of the three components of the magnetic flux density generated by a parallelepiped shaped PM with dimensions ($x_2 - x_1$, $y_2 - y_1$, $z_2 - z_1$) and magnetization (M) oriented along the z-axis. The origin of the reference frame is located at the center of the PM and (x, y, z) are the coordinates of the point considered for magnet flux density computation.

The expressions of the magnetic and electromagnetic forces exerted on the MPM are given by Equations (2) and (3), respectively [34]. In Equation (2), σ_m is the surface charge density, $\mathbf{B}_{ext\ FPM}$ the magnetic flux density from the FPMs, and S is the surface of the MPM poles. In Equation (3), I is the current through a wire surrounded by the external flux density ($\mathbf{B}_{ext\ MPM}$) from the MPM.

$$
\begin{aligned}
B_x(x,y,z) &= \frac{\mu_0 M}{4\pi}\sum_{k=1}^{2}\sum_{m=1}^{2}(-1)^{k+m}\ln\left(F\left(x,y,z,x_m,y_1,y_2,z_k\right)\right)\\
B_y(x,y,z) &= \frac{\mu_0 M}{4\pi}\sum_{k=1}^{2}\sum_{m=1}^{2}(-1)^{k+m}\ln\left(H\left(x,y,z,x_1,x_2,y_m,z_k\right)\right)\\
B_z(x,y,z) &= \frac{\mu_0 M}{4\pi}\sum_{k=1}^{2}\sum_{n=1}^{2}\sum_{m=1}^{2}(-1)^{k+n+m}\\
&\quad\times\tan^{-1}\left(\frac{(x-x_n)(y-y_m)}{(z-z_k)}\,g\left(x,y,z;x_n,y_m,z_k\right)\right)
\end{aligned}
\tag{1}
$$

$$F\left(x,y,z,x_m,y_1,y_2,z_k\right)=\frac{\left(y-y_1\right)+\left[\left(x-x_m\right)^2+\left(y-y_1\right)^2+\left(z-z_k\right)^2\right]^{1/2}}{\left(y-y_2\right)+\left[\left(x-x_m\right)^2+\left(y-y_2\right)^2+\left(z-z_k\right)^2\right]^{1/2}}$$

$$H\left(x,y,z,x_1,x_2,y_m,z_k\right)=\frac{\left(x-x_1\right)+\left[\left(x-x_1\right)^2+\left(y-y_m\right)^2+\left(z-z_k\right)^2\right]^{1/2}}{\left(x-x_2\right)+\left[\left(x-x_2\right)^2+\left(y-y_m\right)^2+\left(z-z_k\right)^2\right]^{1/2}}$$

$$g\left(x,y,z;x_n,y_m,z_k\right)=\frac{1}{\left[\left(x-x_n\right)^2+\left(y-y_m\right)^2+\left(z-z_k\right)^2\right]^{1/2}}$$

$$\mathbf{F}_{Magnetic}=\oint_S \sigma_m \mathbf{B}_{ext\ FPM}\,ds \tag{2}$$

$$\mathbf{F}_{Electromagnetic}=I\int_{wire} d\mathbf{l}\times\mathbf{B}_{ext\ MPM} \tag{3}$$

In the model, the adhesion and friction phenomena (Coulomb friction) are considered for the computation of the MPM displacement. Two contact areas are considered: the first one between the MPM (gold coated) and the thin glass layer (horizontal contact), and the second one between the MPM and the lateral stop (aluminum) (vertical contact). The expression of the friction forces for the horizontal (F_{HF}) and the vertical (F_{VF}) contact areas are given by Equations (4) and (5) respectively, where W is the weight of the mobile part (MPM + potential added mass), F_z is the vertical electromagnetic force exerted on MPM when it is misaligned with the driving wire, $F_{Holding}$ is the magnetic holding force exerted by the FPMs on the MPM, and $\mu_{HF\ dyn}$ and $\mu_{VF\ dyn}$ are the dynamic friction coefficients for the horizontal and vertical contact areas, respectively. When the MPM is misaligned with the supplied wire, the magnetic flux density from the MPM is not totally oriented along the z-axis near the wire. There is a horizontal component (along x or y-axis) of the magnetic flux density which generates a vertical component (F_z) of the electromagnetic force. The adhesion and friction coefficients considered in the model have been experimentally measured using an inclined plane technique (horizontal contact: $\mu_{HF\ static}$ = 0.45, $\mu_{HF\ dyn}$ = 0.41; vertical contact: $\mu_{VF\ static}$ = 0.39, $\mu_{VF\ dyn}$ = 0.35).

$$\mathrm{F_{HF}}=\left(\mathrm{W}-\mathrm{F_z}\right)\cdot\mu_{\mathrm{HF}} \tag{4}$$

$$\mathrm{F_{VF}}=\mathrm{F_{Holding}}\cdot\mu_{\mathrm{VF}} \tag{5}$$

The MPM displacement is computed using Newton's second law (6), where $\mathbf{F}_{Total}$ is the sum of the magnetic and electromagnetic forces exerted on the MPM, M and **d** are the mass and the displacement of the mobile part (MPM + potential added mass), respectively.

$$\sum\mathbf{F}=\mathbf{F}_{\mathrm{Total}}-\mathbf{F}_{\mathrm{HF}}-\mathbf{F}_{\mathrm{VF}}=\mathrm{M}\frac{\mathrm{d}^2\mathbf{d}}{\mathrm{dt}^2} \tag{6}$$

The Figure 2a represents the horizontal components (x and y) of the total force ($\mathbf{F}_{Total}$) exerted on the MPM as function of its position between two discrete positions (located at ±0.5 mm) for different driving current values (0 A, 3 A, and 5 A). The forces obtained using the two wires (TW or BW) are represented. When there is no driving current (0 A), the total force exerted on the MPM is due to the magnetic holding

force only. The holding force value of ±1 mN is then visible when the MPM is in discrete positions (±0.5 mm). When the MPM is in the central position (0 mm), the total force exerted on it is null because the magnetic attractions of the FPMs are perfectly equilibrated. When a driving current is used, the initial curve is upward shifted. The shift corresponds to the added electromagnetic driving force. The value of the electromagnetic forces obtained with the TW and BW are given in Table 1. The electromagnetic force obtained with the BW is 7.1% lower than the one obtained with the TW due to the distance between the two wires ($d_3 - d_2$).

An important property of a digital actuator is that, under standard conditions, the mobile part should not stop in an intermediate position located between the discrete positions [9]. For the presented actuator, if the provided energy is not enough (pulse duration too short and/or current magnitude too small), the MPM can stop between the two discrete positions due to the friction between the MPM and the fixed part. This effect is shown in Figure 2b, where the MPM position as function of time with a 3 A driving current is represented for different pulse durations and using the TW (straight lines) and BW (dashed lines) to switch. If the pulse duration is shorter than 15 ms, the MPM does not reach the +0.5 mm discrete position. For the pulse durations of 8 ms and 12 ms, the MPM displacement is more important using the TW (0.26 mm for 8 ms and 0.71 mm for 12 ms) than using the BW (0.19 mm for 8 ms and 0.51 mm for 12 ms) because the driving force generated using the TW is higher than using the BW. With pulse duration of 22 ms, the switching time is lower than the pulse duration, the MPM velocity increases then throughout the switch. With this configuration, the energy consumption is obviously not minimal. A minimization of the energy consumption can be obtained if the pulse stops before the end of the switch and so that the MPM velocity is high enough to reach the target discrete position (see the switch obtained using the BW for a pulse duration of 15 ms). Considering this configuration, the minimal pulse duration values and the corresponding switching times have been determined and are given in Table 2.

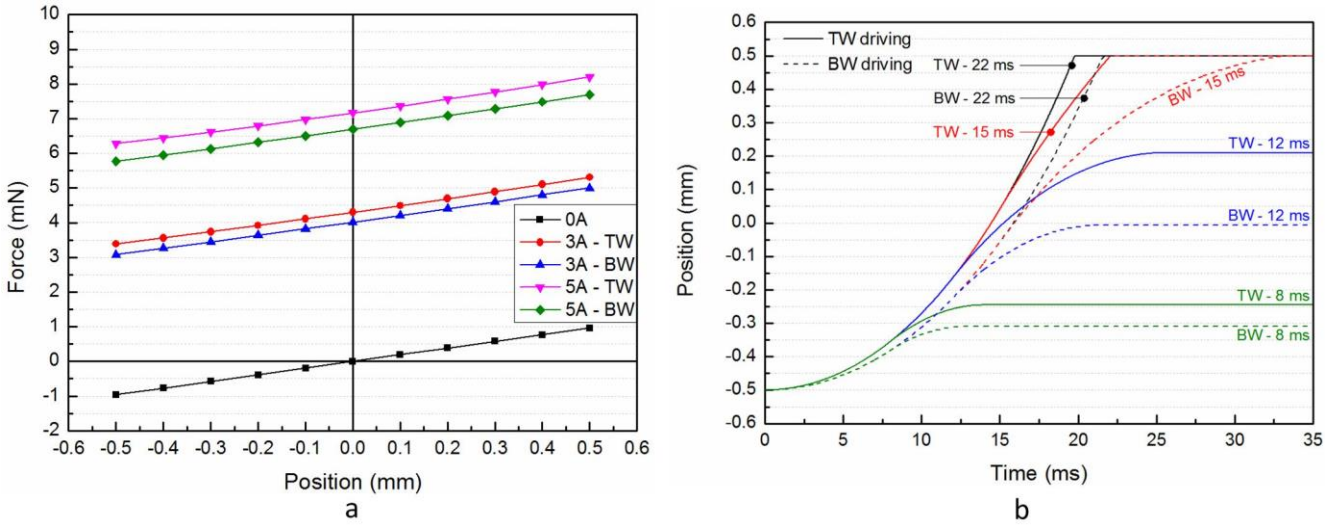

Figure 2. Simulation results: (**a**) force exerted on the MPM as function of its position and for different driving current values, and (**b**) displacement curves of the MPM for different pulse durations.

Table 2. Minimal pulse duration and corresponding switching time.

Driving Current	Minimal Pulse Duration		Switching Time	
	TW	BW	TW	BW
3 A	13.2 ms	15.0 ms	33.3 ms	34.6 ms
4 A	8.5 ms	9.4 ms	30.6 ms	31.8 ms
5 A	6.3 ms	6.9 ms	29.1 ms	30.0 ms
6 A	5.0 ms	5.5 ms	28.2 ms	28.9 ms
7 A	4.2 ms	4.5 ms	27.2 ms	27.9 ms

Considering the values given in Table 2, the energy consumption of the presented digital actuator has been computed for different driving current values and for the two displacement axes (Figure 3a). The energy consumption (E) has been determined with Equation (7) where $U_{Driving}$ is the voltage applied to the considered wire, $I_{Driving}$ is the driving current through the driving wire and Δt is the minimal pulse duration (given in Table 2).

$$E = \left(U_{Driving} \cdot I_{Driving} \right) \cdot \Delta t \quad (7)$$

For a given driving current value, the energy consumption is always higher using the BW than the TW because the electromagnetic force generated is lower using the BW than the TW. The two curves present the same evolution and an optimal value is visible at 2.6 A and 3.0 A for the TW and BW, respectively. For driving current lower than these optimal values, the pulse durations increase sharply compared to the reduction of the driving current values. For driving currents higher than these optimal values, the increase of the driving current generates an increase of the energy consumption more important than the decrease due to the reduction of the pulse duration. For the optimal driving current values, the minimal energy consumption of the digital actuator is 19.1 mJ and 21.9 mJ for the x-axis (TW driving) and the y-axis (BW driving) respectively.

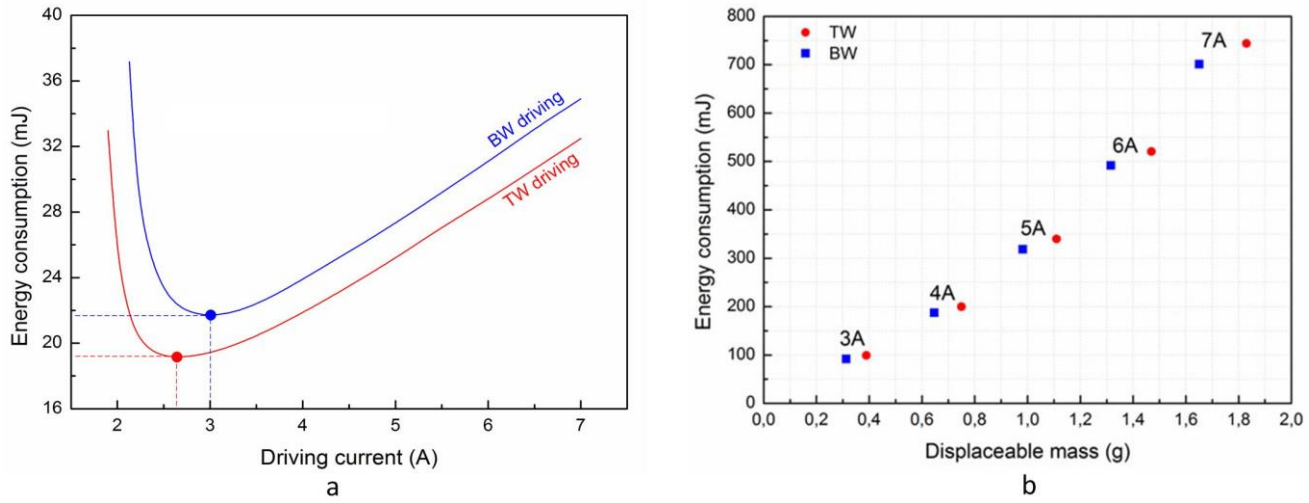

Figure 3. Simulation results: (**a**) energy consumption as function of the driving current value and (**b**) energy consumption as function of the displaceable mass for different driving current values.

Using the model, the maximum displaceable mass has been determined for different driving current values and for the two displacement axes (Figure 3b). The maximal displaceable mass by the MPM is obtained with the highest experimentally-available current value (7 A) and is 1.83 g and 1.65 g using the TW and BW, respectively. For each driving current value, the energy consumption has also been computed considering these added masses. For a given current value (e.g., 7 A), the pulse duration is indeed higher for the TW (95.4 ms) than for the BW (89.9 ms) because of the higher added mass (1.83 g for TW and 1.65 g for BW).

4. Experimentation

4.1. Experimental Setup

Using the presented model, an experimental prototype has been designed and then manufactured. The functional block diagram of the experimental setup is shown in Figure 4a. A Labview interface is used to control the actuator via a data acquisition board NI 6733 (National Instrument) and two voltage-to-current convertors (linear conversion, sampling rate of 50 kHz, input [–10 V; +10 V] and output [–7 A; +7 A]). With a finalized version of the actuator, a binary control with digital outputs of a data acquisition board can be used. However, in the objective to characterize the prototype, different controlling (driving and holding) current values have been used to observe their influences on the actuator behavior. Two analog voltage signals have then been generated using the data acquisition board and converted into current signals by the two voltage-to-current convertors. The actuator prototype is shown in Figure 5b. A miniature optical sensor has been used to characterize the actuator. This sensor has been chosen due to its contactless measurement technique in order to not disturb the MPM displacement, its compact size (diameter of the sensor probe = 2 mm) and its high resolution (several nanometers) [35]. During experimentation, an optical sensor probe has been placed in front of a mirror fixed on the top side of the MPM. The optical probe consists of a bundle of five fibers (one emission fiber located at center and four reception fibers situated around the emission one). The emission fiber emits light on the mirror which is collected by reception fibers and converted into a voltage which is a function of the distance between the fixed probe and the moving mirror. The working principle of this sensor is described in detail in [35]. During experimentation, the output voltage has been recorded using a second data acquisition board NI 6036E.

4.2. Comparison between Experimental and Simulated Results

The MPM displacement between two discrete positions has been measured and compared with the simulated results. This measurement has been independently realized along the two displacement axes taking into account different driving and holding currents values. The Figure 5 represents the comparison between the experimental and simulated results for different driving (Figure 5a,c) and holding (Figure 5b,d) current values. Displacements along the *x*-axis (Figure 5a,b) and *y*-axis (Figure 5c,d) are presented. In Figure 5a,c, the driving current varies and there is no holding current. In Figure 5b,d, the driving current is fixed at 5 A and the holding current varies from 0 A to 7 A. In Figure 5d, the result with a holding current of 7 A is not represented because with this value, the MPM can indeed not switch along the *y*-axis due to the high friction force. A measurement artifact is visible on experimental results when the MPM

reaches the discrete position. This artifact corresponds to an orientation of the MPM due to the impact with the stop. This orientation generates a variation of the light collected by the optical sensor which interprets this variation as a linear displacement. In the figure, a decrease of the switching time is visible when the driving current increases (Figure 5a,c). Moreover, an increase of the holding current generates an increase of the switching time because the lateral friction between the MPM and the stop is increased (Figure 5b,d).

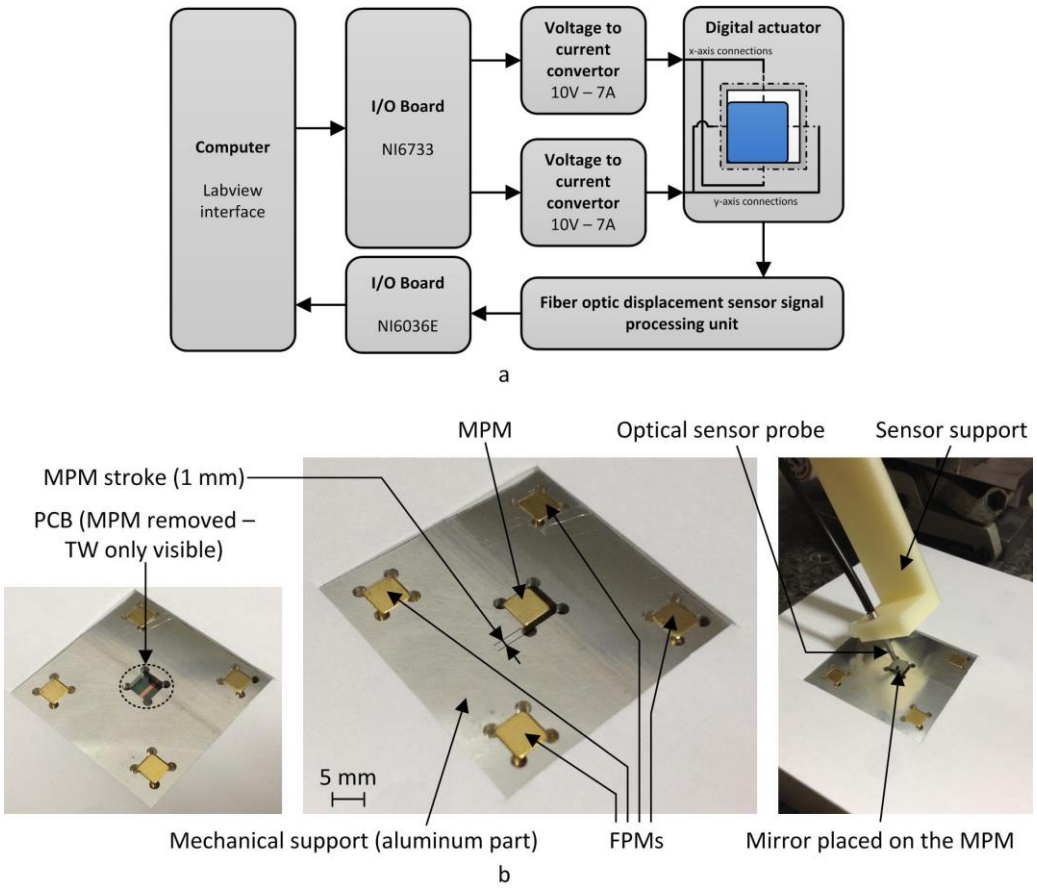

Figure 4. (**a**) Functional block diagram, (**b**) experimental setup.

A comparison between the simulated and experimental times to reach 90% of the actuator stroke (t_{90}) is presented in Figure 6a,b for the *x*- and *y*-axis, respectively. In this figure, t_{90} is represented as function of the driving current value for different holding current values. The influences of the driving and holding current observed previously are clearly visible. The presented comparisons between the simulated and theoretical results show that the model characterizes well the experimental behavior of the actuator for the two displacement axes.

A frequency study has been done by computing the bandwidth of the actuator for displacements along the two axes. Based on the results presented in Figure 5, the experimental rise times (10%–90%) have been determined for different driving current values (between 3 A and 7 A without holding current). The corresponding bandwidth has been determined for each considered configuration and the results are presented in Table 3. With the highest driving current value (7 A), the rise time is minimal (6.7 ms for the *x*-axis and 8.6 ms for the *y*-axis) then the bandwidth is maximal (52.2 Hz for the *x*-axis and 40.7 Hz for the *y*-axis).

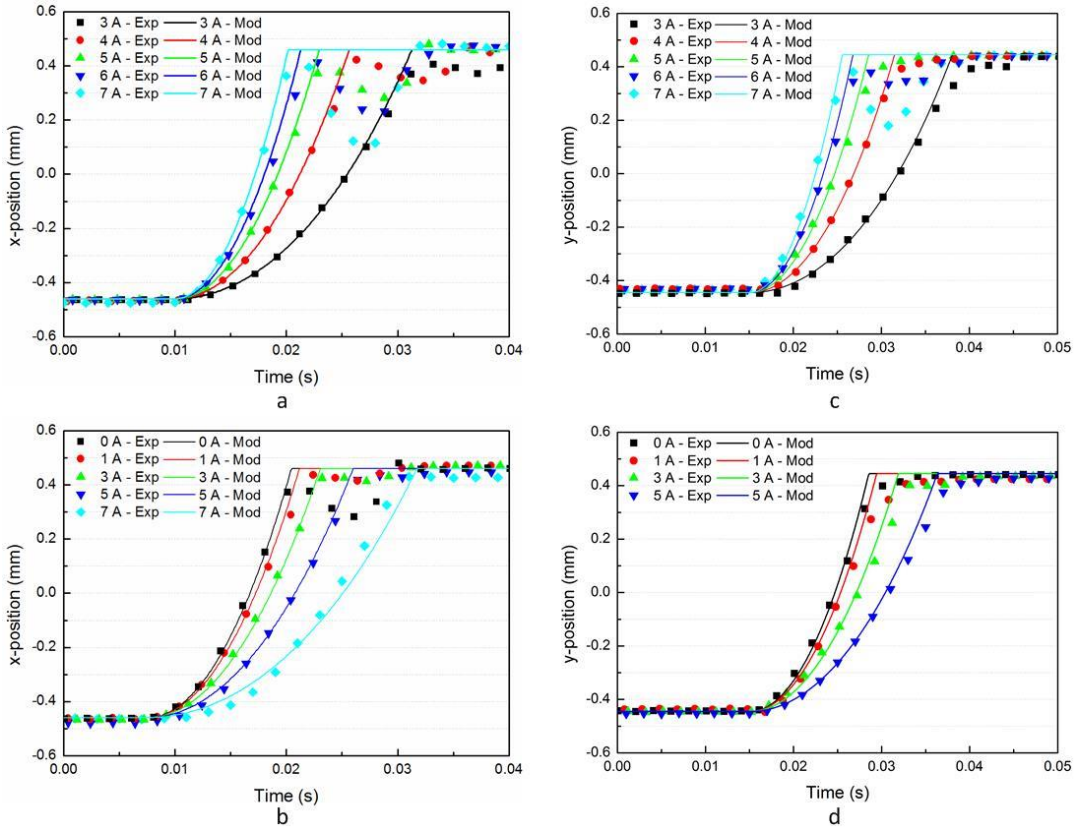

Figure 5. Comparisons between experimental (Exp) and modeled (Mod) MPM displacement: (**a**) influence of driving current without holding current for *x*-axis switching. (**b**) Influence of holding current with 5 A driving current for *x*-axis switching. (**c**) Influence of driving current without holding current for the *y*-axis switching. (**d**) Influence of holding current with 5 A driving current for *y*-axis switching.

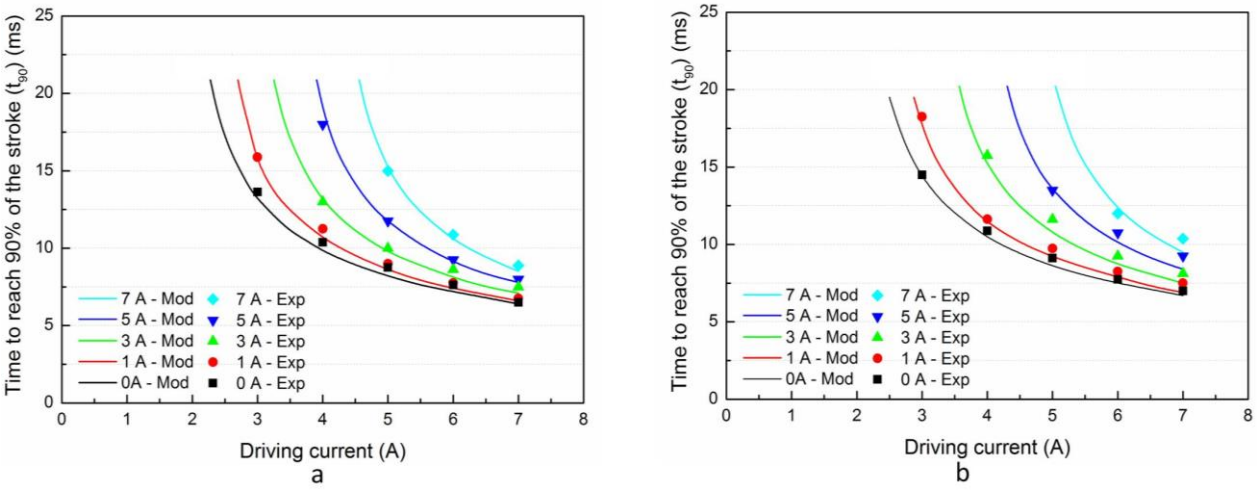

Figure 6. Comparisons between experimental (Exp) and modeled (Mod) rise times: (**a**) rise times for *x*-axis switching, and (**b**) rise times for *y*-axis switching.

Table 3. Bandwidth of the actuator.

Driving Current	Bandwidth	
	***x*-axis**	***y*-axis**
3 A	25.4 Hz	22.3 Hz
4 A	35.0 Hz	29.2 Hz
5 A	41.2 Hz	34.6 Hz
6 A	47.3 Hz	39.3 Hz
7 A	52.2 Hz	40.7 Hz

4.3. Displaceable Mass

The displaceable mass by the MPM has been experimentally measured for different driving current values and compared with the theoretical values determined using the model (see Figure 3b). The comparison for displacement along the *x*- and *y*-axis is presented in Figure 7a,b, respectively. Experimentally, for a given mass, the driving current needed to switch the mobile part (MPM + added mass) has been determined for different initial position in the square cavity and for the two displacement directions. Four measurements have then been done for each experimental configuration (*i.e.*, for *x*-axis: $(-x_{MPM}; -y_{MPM}) \rightarrow (+x_{MPM}; -y_{MPM})$, $(+x_{MPM}; -y_{MPM}) \rightarrow (-x_{MPM}; -y_{MPM})$, $(-x_{MPM}; +y_{MPM}) \rightarrow (+x_{MPM}; +y_{MPM})$, $(+x_{MPM}; +y_{MPM}) \rightarrow (-x_{MPM}; +y_{MPM})$). The minimum and maximum current values obtained are represented by a horizontal error bar for each experimental point. This variation is due, on one hand, to inhomogeneous holding force between the discrete positions because of manufacturing errors and on the other hand, to inhomogeneous friction conditions between the MPM and the fixed part of the actuator. For the two displacement axes, the model characterizes well the experimental results. Considering the horizontal bars in the figure, three zones have been determined to characterize the actuator behavior. Zone I is the non-functioning zone where the MPM cannot switch properly because the driving current is not enough high. Zone III is the normal functioning zone where the switch of the MPM is certain to be obtained. Between these two zones, an uncertainty zone called Zone II, is defined in which the switch of the MPM is uncertain due to inhomogeneous holding and friction forces.

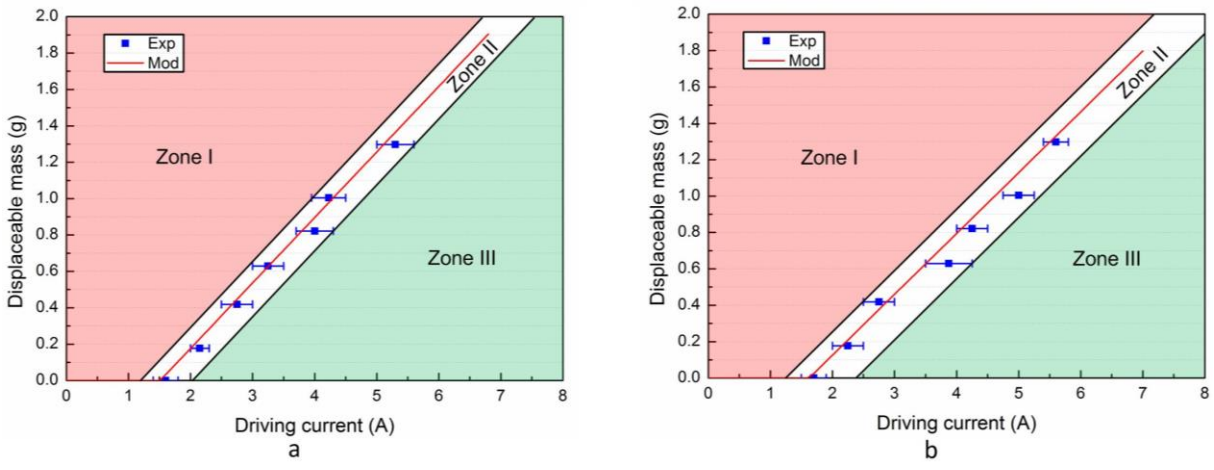

Figure 7. Comparisons between experimental (Exp) and modeled (Mod) displaceable mass for different driving current values: (**a**) displacement along *x*-axis switching, and (**b**) displacement along *y*-axis switching.

4.4. Positioning Repeatability Error

The positioning repeatability of the MPM in discrete positions has been measured in order to characterize the high-precision property and the digital behavior of the presented actuator. In that objective, four optical sensor probes have been used: two probes for the *x*-positioning repeatability errors (+*x* and –*x*) and two probes for the *y*-positioning repeatability errors (+*y* and –*y*). In this configuration, the limit of resolution of the optical sensors is 10 nm. Since the actuator has two displacement directions, two components of the positioning repeatability error have been measured: the positioning repeatability error along the displacement direction, called axial positioning repeatability error (APR error), and the positioning repeatability error orthogonal to the displacement direction, called lateral positioning repeatability error (LPR error) (Figure 8). Twenty-four switches between two discrete positions have been experimentally realized. For a considered error (for example APR), the standard deviations on the two discrete positions (along the displacement direction) have been computed and the positioning repeatability (APR) error has been defined as the maximum value of these two standard deviations. The APR and LPR positioning repeatability errors have then been measured along the two displacement axes for different holding current values and are presented in Figure 9a,b, respectively. The two repeatability errors are clearly reduced when the holding current increases. When the holding current changes from 0 A to 1 A, the APR and LPR errors are reduced by 40% and 76%, respectively. The influence of the holding current is more important on the LPR than on the APR. This phenomenon was expected because the holding force, generated by the holding current, ensures the contact between the MPM and the lateral stop then reduces directly the LPR error. An increase of the holding current from 1 A to 3 A reduces the APR and LPR errors by 53% and 65%, respectively. With the highest holding current value (7 A), the APR and LPR errors represent 111 nm and 74 nm, respectively. The presented high precision digital actuator is then able to realize discrete displacement with a positioning repeatability error lower than 0.01% of its stroke. From the energy consumption point of view, a 3 A holding current seems to be an optimal value because compared to the configuration with 7 A, the holding current is increased by 233% but the APR and LPR errors are only reduced by 47% and 10%, respectively.

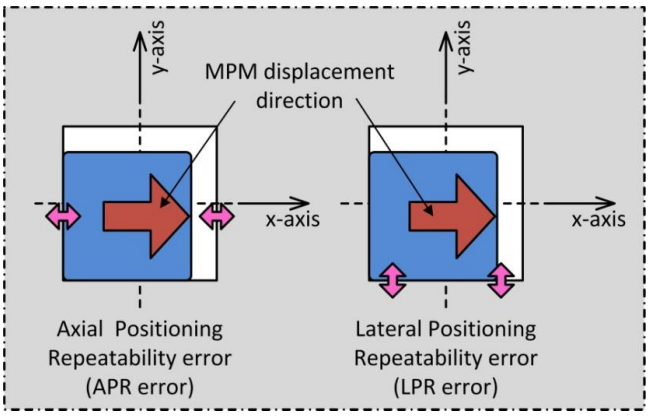

Figure 8. Representation of the axial positioning repeatability error (APR error) and of the lateral positioning repeatability error (LPR error).

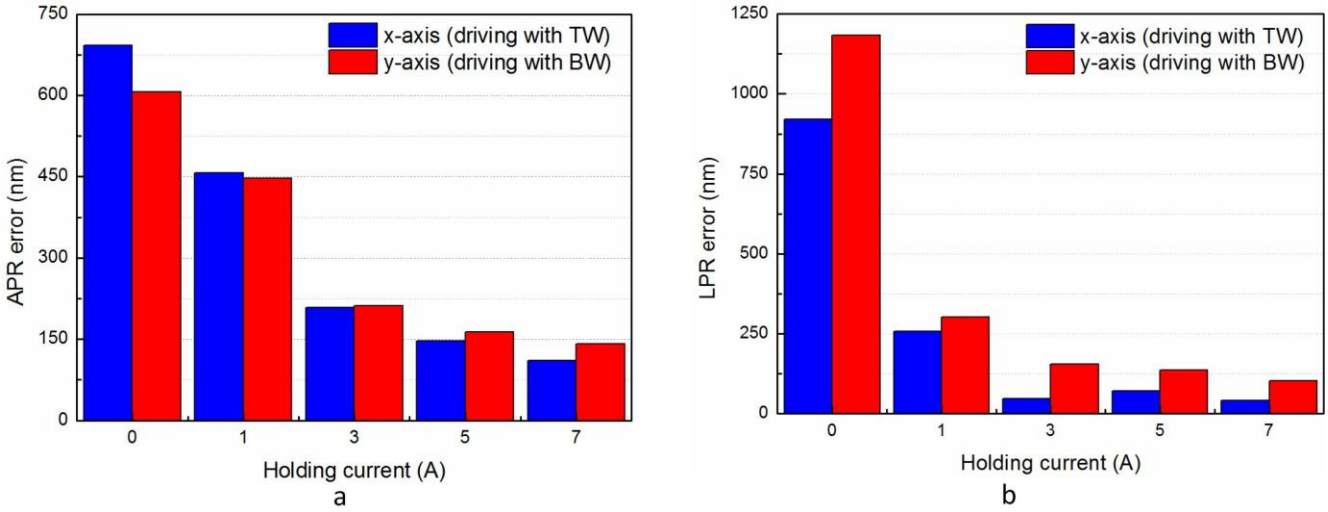

Figure 9. Repeatability errors as function of the holding current value: (**a**) APR error, and (**b**) LPR error.

In order to highlight the holding function of the FPMs, the positioning repeatability errors have also been measured without them. In this case, the APR and LPR errors represent 2700 nm and 11,000 nm, respectively. The APR and LPR errors are then reduced by 71% and 91%, respectively when the FPMs are present (values of the APR and LPR errors given in Figure 8). This result proves that the presence of the FPMs has a very high influence on the high precision property of the actuator.

4.5. Comparison with Existing Actuators

A comparison of the properties and performances (*i.e.*, dimensions, number of discrete positions, energy consumption, generated force, stroke, and the ratio between energy and stroke) between the presented actuator and existing digital actuators is provided in Table 4. Compared to existing actuators, the presented one is among those having the largest dimensions. However, these dimensions allow long stroke and bi-dimensional motions. This 2D architecture allowing planar motions represents the main interest of the presented actuator because a large majority of digital actuators are limited to only two discrete positions. In literature, some digital actuators having more than two discrete positions have, however, been developed. For example, the device developed by Han *et al.* has the same properties as the presented actuator (2D displacement with a 1 mm stroke) but with larger dimensions. The actuator developed by Oberhammer *et al.* has very small dimensions but with an architecture limited to only three positions. Due to these big dimensions, the energy consumption of the presented actuator is also among the most important. Taking into account the stroke, the presented actuator proposes, however, an interesting ratio between energy and stroke compared to other existing actuators. Finally, the square shape of the presented actuator is quite adapted to realize actuator arrays because it can easily cover a surface. The realization of a micro-fabricated actuator array based on the presented architecture is indeed a perspective of this work.

Table 4. Comparison of performances between existing and the presented actuators.

Actuator	Dimensions	Number of Positions	Energy Consumption	Generated Force	Stroke	Energy/Stroke Ratio
Staab *et al* [36]	0.24 cm^2	2	1.6 mJ	17 mN	≈100 µm	16 mJ/mm
Fu *et al* [37]	1.6 cm^2	2	58 mJ	0.07 mN	50 µm	1160 mJ/mm
Dieppedale *et al* [38]	0.0004 cm^2	2	0.048 mJ	/	≈10 µm	5 mJ/mm
Miao *et al* [19]	0.36 cm^2	2	25 mJ	/	380 µm	66 mJ/mm
Oberhammer *et al* [23]	≈0.006 cm^2	3	/	1.1 mN	≈±10 µm	/
Han *et al* [39]	56 cm^2	4	/	/	1 × 1 mm^2	/
Presented actuator	10.9 cm^2	4	19.1 mJ	10.2 mN	1 × 1 mm^2	19 mJ/mm

5. Application

An application of the digital actuator is presented in this section. This application consists of a linear conveyor able to realize long displacement and takes advantage of the high precision and of the two displacement directions of the actuator. In this application, two rack gears are used (Figure 10a): rack gear 1 is placed on the top side of the actuator, which corresponds to the mobile part of the conveyor, and rack gear 2 is fixed on the top side of the MPM. During the functioning of the conveyor, the two rack gears can be engaged or disengaged as represented in Figure 10b. The high precision of the digital actuator is an important property for this application because it ensures the engaging/disengaging of the two rack gears without fail at each step. When the two rack gears are engaged, the movement of the MPM generates a displacement of the conveyor mobile part (rack gear 1). For this application, two orthogonal displacement directions are needed: one direction for the actuation and one for the engaging/disengaging of the two rack gears. With the same current value, the electromagnetic force generated with the TW (*x*-axis switching) is higher than with the BW (*y*-axis switching). The *x*-axis has then been chosen for the actuation direction because a high actuation force can be necessary if the mass of the conveyed part is important. On the other hand, the required force during the engaging/disengaging phases is smaller so that the *y*-axis (switching using the BW) has been used for this direction.

An experimental test has been realized to validate the principle of this linear conveyor. The two rack gears have been manufactured using rapid prototyping techniques and are shown in Figure 10c. The geometrical properties of the two rack gears and teeth are given in Table 5. In order to facilitate the engaging/disengaging phases, the teeth have a trapezoidal shape. Eight apertures have been fabricated in rack gear 1 in order to reduce its mass and to see the displacement of rack gear 2 during the functioning (visible in Figure 11a).

The Figure 11 represents a displacement sequence with the experimental prototype. This sequence is composed of four steps. In the initial position, the two rack gears are disengaged and the MPM is located in the ($-x_{MPM}$; $-y_{MPM}$) discrete position (Figure 11a). At the first step, the MPM switches in the $+y$ direction and reaches the ($-x_{MPM}$; $+y_{MPM}$) discrete position (Figure 11b) in order to engage the two rack gears. At the second step, the MPM switches in the $+x$ direction and reaches the ($+x_{MPM}$; $+y_{MPM}$) discrete position (Figure 11c). During this step, the rack gear 1 is moved from a distance corresponding to the MPM stroke. At the third step, the two rack gears are disengaged then the MPM switches in the $-y$ direction and reaches the ($+x_{MPM}$; $-y_{MPM}$) discrete position (Figure 11d). At the fourth step, the MPM reaches the initial position ($-x_{MPM}$; $-y_{MPM}$) by switching in the $-x$ direction (Figure 11e) then a new

sequence can be realized. A representation of the current signals for *x*-axis switching (TW) and *y*-axis switching (BW) used for the displacement sequence are presented in Figure 11f,g, respectively. During the sequence, driving and holding currents are used in order to ensure properly the engaging/disengaging of the two rack gears and the displacement of the rack gear 1. Using this experimental setup, displacements of 30 mm (using the total length of rack gear 1) and a displacement velocity up to 7.5 mm/s have been achieved.

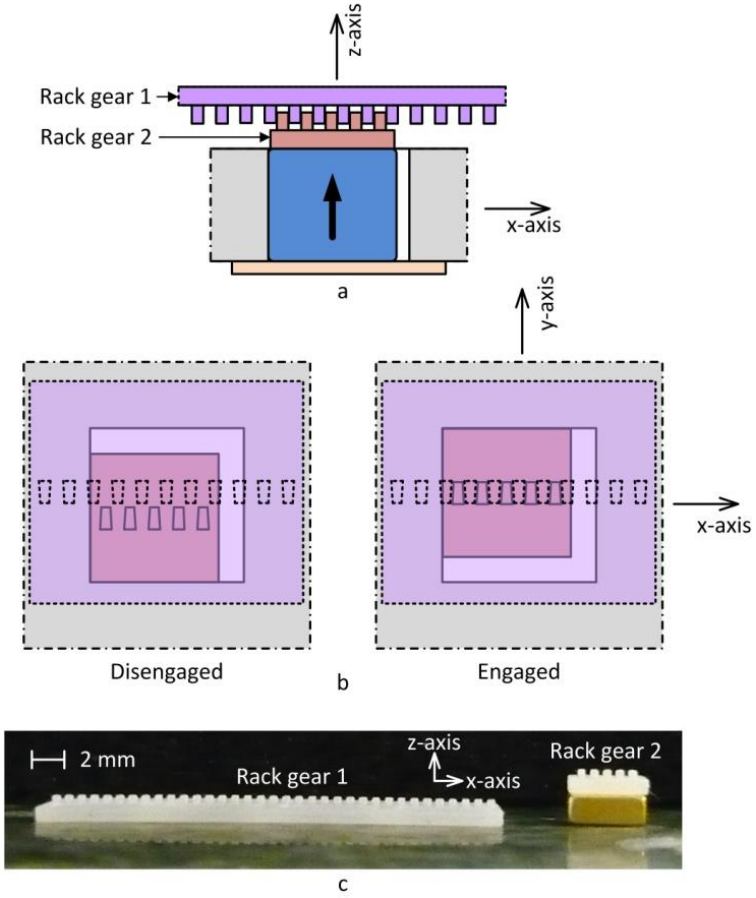

Figure 10. Principle of a linear conveyor based on the digital actuator: (**a**) side view, (**b**) top view, (**c**) picture of the two rack gears.

Table 5. Rack gears properties.

Rack gears dimensions		
	Rack gear 1	Rack gear 2
Length (along x-axis)	30 mm	5 mm
Width (along y-axis)	10 mm	5 mm
Thickness (along z-axis)	1.5 mm	1.5 mm
Number of teeth	35	5
Pitch	0.85 mm	0.85 mm
Tooth dimensions		
Length (along x-axis)	0.33 mm to 0.36 mm (trapeze shape)	
Width (along y-axis)	0.5 mm	
Thickness (along z-axis)	0.5 mm	

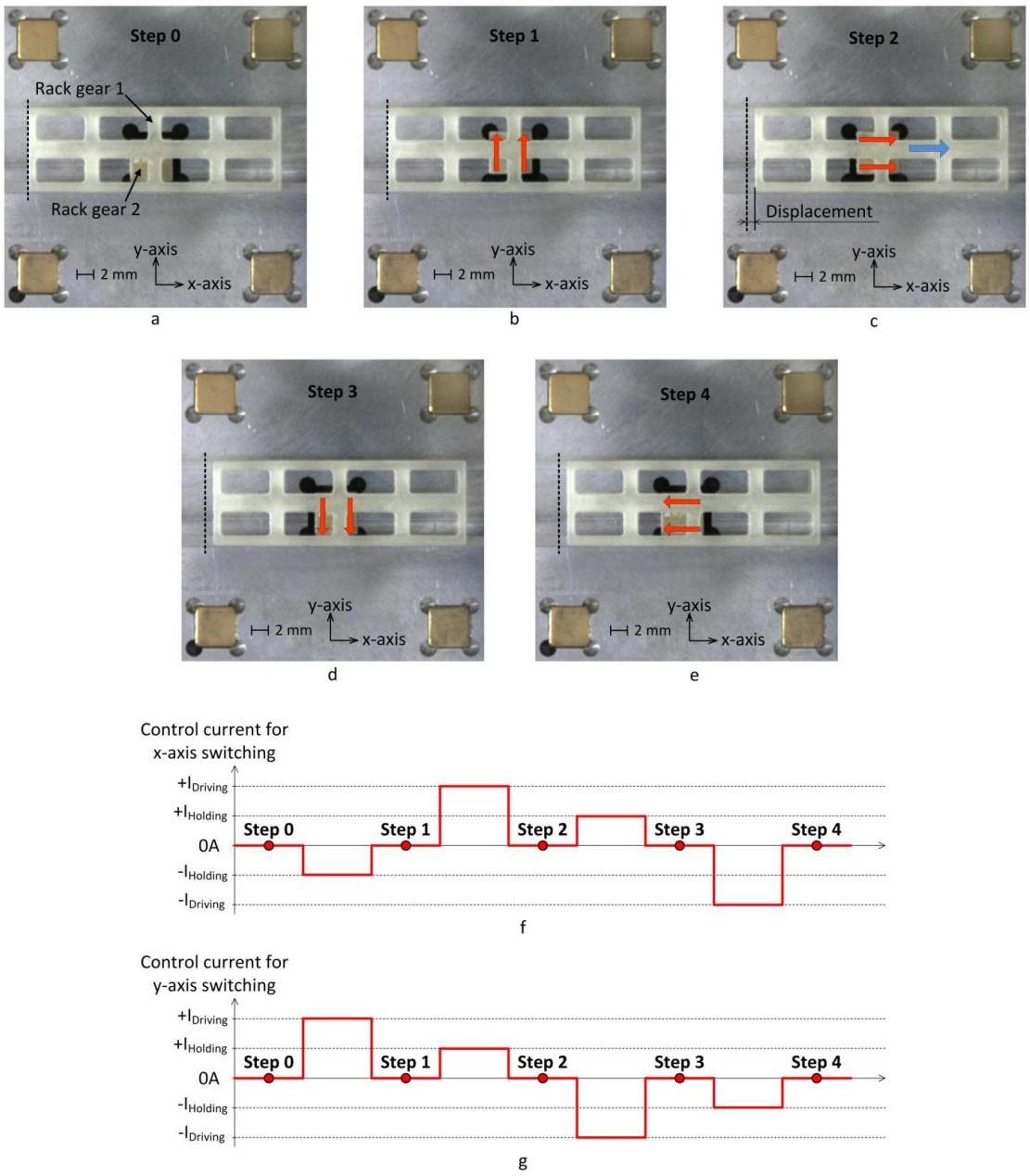

Figure 11. Displacement sequence of the linear conveyor: (**a**, **b**, **c**, **d**, and **e**) pictures of the prototype during the displacement sequence, (**f**) control signal for *x*-axis switching used for the sequence, (**g**) control signal for *y*-axis switching used for the sequence.

6. Conclusion and Perspectives

In this paper, a high-precision digital electromagnetic actuator having two orthogonal displacement axes and four discrete positions is presented. An analytical model of the actuator, which computes the forces exerted on the MPM and determines its displacement between two discrete positions, has been developed. Using the model, the minimal energy consumption (19.1 mJ) and the maximal displaceable mass by the actuator (1.83 g) have been determined. An experimental prototype of the actuator has then been manufactured, tested, and a good agreement between the experimental and simulated results along the two displacement directions has been observed. The high-precision property of the actuator has also been experimentally characterized by measuring the positioning repeatability errors along the

displacement direction (111 nm with 7 A holding current) and orthogonally to this direction (72 nm with 7 A holding current). The actuator is then able to realize a discrete displacement with a positioning repeatability error lower than 0.01% of its stroke. The positive influences of the FPMs and of the holding current have also been observed on these errors. Finally, an example of the application of the digital actuator has been proposed and tested. This application consists of a linear conveyor which takes advantages of the two orthogonal displacement directions: one for actuation step and one for engagement/disengagement step. An experimental test of this conveyor has been realized and long stroke (30 mm) with high velocity (7.5 mm/s) have been reached.

The main perspective of this work is to develop a digital actuator array realized using micro-fabrication techniques. These techniques will increase the manufacturing quality of the prototype then improve its precision. With this array complex tasks may be realized using the elementary actions of each actuator. One envisaged application consists of a plane displacement device which will take advantage of the two displacement axes of the elementary actuators. To control the plate displacement, dedicated control laws will be developed to realize the desired trajectory while ensuring an additional property as a minimization of the energy consumption or displacement time.

Author Contributions

Laurent Petit proposed the concept of the actuator, designed, modeled, and characterized the experimental prototype; Erwan Dupont designed the conveyor and participated to the experimental characterization; Emmanuel Dor é worked on the development of the analytical model and on the design of the actuator prototype; Fr éd éric Lamarque proposed the experimental characterization technique and participated to the characterization; Christine Prelle supervised the concept of the actuator, participated to the development of the analytical model and supervised the experimental characterization, especially the controlling part.

Conflicts of Interest

The authors declare no conflict of interest.

References

1. Kluk, D.J.; Boulet, M.T.; Trumper, D.L. A high-bandwidth, high-precision, two-axis steering mirror with moving iron actuator. *Mechatronics* **2012**, *22*, 257–270.
2. Du, Z.; Shi, R.; Dong, W. A Piezo-Actuated High-Precision Flexible Parallel Pointing Mechanism: Conceptual Design, Development, and Experiments. *IEEE Trans. Robot.* **2014**, *30*, 131–137.
3. Khan, M.U.; Bencheikh, N.; Prelle, C.; Lamarque, F.; Beutel, T.; Buttgenbach, S. A Long Stroke Electromagnetic XY Positioning Stage for Micro Applications. *IEEE/ASME Trans. Mechatron.* **2012**, *17*, 866–875.
4. Le, Y.; Fang, J.; Sun, J. Design of a Halbach array permanent magnet damping system for high speed compressor with large thrust load. *IEEE Trans. Magn.* **2015**, *51*, 1–9.

5. Chen, S.-L.; Kamaldin, N.; Teo, T.J.; Liang, W.; Teo, C.S.; Yang, G.; Tan, K.K. Towards Comprehensive Modeling and Large Angle Tracking Control of a Limited Angle Torque Actuator with Cylindrical Halbach. *IEEE/ASME Trans. Mechatron.* **2015**, in press.
6. Shen, Y.; Liu, G.Y.; Xia, Z.P.; Zhu, Z.Q. Determination of maximum electromagnetic torque in PM brushless machines having two-segment Halbach array. *IEEE Trans. Ind. Electron.* **2014**, *61*, 718–729.
7. Sun, X.; Chen, W.; Zhang, J.; Zhou, R.; Chen, W. A novel piezo-driven linear-rotary inchworm actuator. *Sens. Actuators A Phys*. **2015**, *224*, 78–86.
8. Ikeda, H.; Morita, T. High-precision positioning using a self-sensing piezoelectric actuator control with a differential detection method. *Sens. Actuators A Phys*. **2011**, *170*, 147–155.
9. Jensen, B.D.; Parkinson, M.B.; Kurabayashi, K.; Howell, L.L.; Baker, M.S. Design optimization of a fully-compliant bistable micro-mechanism. In Proceedings of the 2001 ASME International Mechanical Engineering Congress and Exposition, New York, NY, USA, 11–16 November 2001.
10. Zhang, Y.H.; Ding, G.; Fu, S.; Cai, B. A fast switching bistable electromagnetic microactuator fabricated by UV-LIGA technology. *Mechatronics* **2007**, *17*, 165–171.
11. Wu, Y.; Ding, G.; Zhang, C.; Wang, J.; Mao, S.; Wang, H. Design and implementation of a bistable microcantilever actuator for magnetostatic latching relay. *Microelectron. J.* **2010**, *41*, 325–330.
12. Haddab, Y.; Chalvet, V.; Chen, Q.; Lutz, P. Digital microrobotics using MEMS technology. *Adv. Mechatron. MEMS Devices* **2013**, *23*, 99–116.
13. Petit, L.; Hassine, A.; Terrien, J.; Lamarque, F.; Prelle, C. Development of a Control Module for a Digital Electromagnetic Actuators Array. *IEEE Trans. Ind. Electron.* **2014**, *61*, 4788–4796.
14. Ishii, H.; Ting, K.L. SMA actuated compliant bistable mechanisms. *Mechatronics* **2004**, *14*, 421–437.
15. Cugat, O. *Micro-Actionneurs Electromagnétiques MAGMAS*; Hermès Science Publications: Paris, France, 2002; p. 320.
16. Kim, C.H. Mechanically coupled low-voltage electrostatic resistive RF multithrow switch. *IEEE Trans. Ind. Electron.* **2012**, *59*, 1114–1122.
17. Lee, J.G.; Ryu, J.; Lee, H.; Cho, M. Saddle-shaped, bistable morphing panel with shaped memory alloy spring actuator. *Smart Mater. Struct.* **2014**, *23*, doi:10.1088/0964-1726/23/7/074013.
18. Zaidi, S.; Lamarque, F.; Carton, O.; Prelle, C. Contactless and selective energy transfer to a bistable micro-actuator using laser heated shape memory alloy. *Smart Mater. Struct.* **2012**, *21*, doi:10.1088/0964-1726/21/11/115027.
19. Miao, X.; Dai, X.; Wang, P.; Ding, G.; Zhao, X. Design, fabrication and characterization of a bistable electromagnetic microrelay with large displacement. *Microelectron. J.* **2011**, *42*, 992–998.
20. Petit, L.; Prelle, C.; Dore, E.; Lamarque, F.; Bigerelle, M. A Four-Discrete-Position Electromagnetic Actuator: Modeling and Experimentation. *IEEE/ASME Trans. Mechatron.* **2010**, *15*, 88–96.
21. Giddings, P.F.; Kim, H.A.; Salo, A.I.T.; Bowen, C.R. Modelling of piezoelectrically actuated bistable composites. *Mater. Lett.* **2011**, *65*, 1261–1263.
22. Kang, C.G.; Lee, J.S.; Han, J.H. Development of bi-stable and millimeterscale displacement actuator using snap-through effect for reciprocating control fins. *Aerosp. Sci. Technol.* **2014**, *32*, 131–141.
23. Oberhammer, J.; Tang, M.; Liu, A.Q.; Stemme, G. Mechanically tri-stable, true single-pole-double-throw (SPDT) switches. *J. Micromech. Microeng.* **2006**, *16*, 1–8.

24. Tsai, C.; Tsai, J. MEMS optical switches and interconnects. *Displays* **2015**, *37*, 33–40.
25. Al Hajjar, H.; Petit, L.; Lamarque, F.; Fracasso, B. 1 ×4 Optical Switch Based on Digital Actuator. *Int. J. Optomechatron.* **2015**, *9*, 141–150.
26. Jien, S.; Hirai, S.; Honda, K. Miniaturized unconstrained on-off pneumatic poppet valve—Experiment and simulation. *IEEE/ASME Trans. Mechatron.* **2009**, *14*, 626–635.
27. Moreno, J.M.; Quero, J.M. A novel single-use SU-8 microvalve for pressure-driven microfluidic applications. *J. Micromech. Microeng.* **2010**, *20*, doi:0.1088/0960-1317/20/1/015005.
28. Matsunaga, T.; Totsu, K.; Esashi, M.; Haga, Y. Tactile display using shape memory alloy micro-coil actuator and magnetic latch mechanism. *Displays* **2013**, *34*, 89–94.
29. Han, W.; Cho, Y.C. High-Precision Digital-to-Analog Tunable Capacitors with Improved Quality Factor Using a Parallel Digital Actuator Array. *J. Microelectromech. Syst.* **2009**, *18*, 773–783.
30. Chouinard, P.; Plante, J. Bistable Antagonistic Dielectric Elastomer Actuators for Binary Robotics and Mechatronics. *IEEE/ASME Trans. Mechatron.* **2012**, *17*, 857–865.
31. Fukuta, Y.; Chapuis, Y.A.; Mita, Y.; Fujita, H. Design, fabrication, and control of MEMS-based actuator arrays for air-flow distributed micromanipulation. *J. Microelectromech. Syst.* **2006**, *15*, 912–926.
32. Ataka, M.; Legrand, B.; Buchaillot, L.; Collard, D.; Fujita, H. Design, Fabrication, and Operation of Two-Dimensional Conveyance System with Ciliary Actuator Arrays. *IEEE/ASME Trans. Mechatron.* **2009**, *14*, 119–125.
33. Petit, L.; Prelle, C.; Dorée, E.; Lamarque, F.; Bigerelle, M. Optimized design of a four discrete positions electromagnetic actuator. In Proceedings of the IEEE International Conference on Mechatronics, Malaga, Spain, 14–17 April 2009; pp. 1–6.
34. Furlani, E.P. *Permanent Magnet and Electromechanical Devices—Materials, Analysis and Applications*; Academic Press: San Diego, CA, USA, 2001; p. 518.
35. Prelle, C.; Lamarque, F.; Revel, P. Reflective optical sensor for long-range and high-resolution displacements. *Sens. Actuators A Phys*. **2006**, *127*, 139–146.
36. Staab, M.; Schlaak, H.F. Novel electrothermally actuated magnetostatic bistable microrelay for telecommunication applications. In Proceedings of the IEEE 24th International Conference on Micro Electro Mechanical Systems (MEMS), Cancun, Mexico, 23–27 January 2011; pp. 261–264.
37. Fu, S.; Ding, G.; Wang, H.; Yang, Z.; Feng, Z. Design and fabrication of a magnetic bi-digital electromagnetic MEMS relay. *Microelectron. J.* **2007**, *38*, 556–563.
38. Dieppedale, C.; Desloges, B.; Rostaing, H.; Delamare, J.; Cugat, O.; Meunier-Carus, J. Magnetic bistable micro-actuator with integrated permanent magnets. In Proceedings of IEEE Sensors 2004, Vienne, Austria, 24–27 October 2004; pp. 493–496.
39. Han, J.S.; Müller, C.; Wallrabe, U.; Korvink, J.G. Design, Simulation, and Fabrication of a Quadstable Monolithic Mechanism with X- and Y- Directional Bistable Curved Beams. *ASME J. Mech. Design* **2007**, *129*, 1198–1203.